Reducing Grain-Boundary Resistivity of Copper Nanowires by Doping

Mathieu César,[1] Daniel Gall,[2] and Hong Guo[1]
[1]Centre for the Physics of Materials and Department of Physics, McGill University, Montréal, Québec H3A 2T8, Canada
[2]Department of Materials Science & Engineering, Rensselaer Polytechnic Institute, Troy, New York 12180, USA
(Received 9 February 2016; revised manuscript received 19 April 2016; published 25 May 2016)

The resistance of doped single grain boundaries (GBs) in copper is calculated from first principles and systematically compared to its pure single GB equivalent. As a first step, a state-of-the-art *ab initio* method is used to calculate the resistivity of doped bulk copper for 16 doping elements at concentration 1 at. %. Results are in qualitatively excellent and quantitatively reasonable agreement with the corresponding experimental data, and allow us to determine Ag, Zn, Mg, Pd, Al, and In as best candidates for GB doping. These atoms have a minimal impact on the bulk resistivity, while they also conform to a set of established criteria for alloying with copper. Then, the specific resistivity of six twin GBs is determined for these elements over a wide spectrum of doping concentrations for the submonolayer and the monolayer GB complexions. Reduced resistivity is observed for Zn, Mg, Al, In, and other elements in two high-Σ GBs, and is qualitatively related to the segregation enthalpy as well as to a low number of empty states around the Fermi energy in the boundary plane region of the GB. The results indicate the possibility for a reduced net resistivity in copper interconnects by GB doping.

DOI: 10.1103/PhysRevApplied.5.054018

I. INTRODUCTION

The downscaling of integrated circuits is presently limited by the large increase of resistivity observed in copper interconnects as the linewidth becomes close to or smaller than 39 nm, the electron mean free path of the material. This is the well-known size effect [1–3]. It was shown that a requirement for the effective resistivity of 2.2 $\mu\Omega\,$cm cannot be attained at 50-nm linewidth and less, even with cooling, as the size effect is temperature independent [4,5]. Instead, resistivities of 4.5 $\mu\Omega\,$cm and up are measured at this feature scale [1,4–6], which is more than twice the international annealed copper standard, 1.724 $\mu\Omega\,$cm. As the copper interconnect technology will remain dominant in the near future while integrated circuits are scaled further down [7], efforts must be undertaken to limit or diminish line resistivity in the size-effect regime.

One of the major contributions to the resisitivity in the size-effect regime is grain-boundary (GB) scattering [1–3]. It is found to roughly account for 40% of the total resistivity in copper wires over the technology nodes ranging from 32 to 7 nm [8]. The resistivity ρ of a polycrystalline film is traditionally understood in terms of the Mayadas-Schatzkes model [9]:

$$\frac{\rho}{\rho_0} = \left[1 - \frac{3}{2}\alpha + 3\alpha^2 - 3\alpha^3 \ln\left(1 + \frac{1}{\alpha}\right)\right]^{-1}, \qquad (1)$$

where ρ_0 is the bulk resistivity and α is defined as

$$\alpha = \left(\frac{r}{1-r}\right)\frac{\lambda}{g}, \qquad (2)$$

λ being the electron mean free path, g the average grain size, and r the average GB reflection coefficient which varies from 0 for total transmission to 1 for total reflection. In the limiting case $\alpha \ll 1$, Eq. (1) simplifies to

$$\frac{\rho}{\rho_0} = 1 + \frac{3}{2}\left(\frac{r}{1-r}\right)\frac{\lambda}{g}. \qquad (3)$$

This model has since been refined [10–12]. However, it still relies in its essence on the two parameters g and r. According to Eq. (3), one way of reducing the resistivity in a given material is by increasing its average grain size g, the case of a single crystal with infinite g being ideal. The grain size is usually limited by the smallest dimension (width or height) in interconnects [13] and approaches to control the grain-boundary density have been proposed [14–16], while the possibility of grain growth using the conventional annealing process seems limited in very narrow interconnects [17]. On another side, it should be possible to reduce the resistivity of a material by reducing its average GB reflection coefficient r. This parameter is usually obtained as an empirical quantity that averages out the effect of all the GBs present in the material, as the reflection coefficient is in fact strongly tied to the GB structure. Enhancing the fraction of low-resistivity GBs, such as coherent twin boundaries, is one way to address the problem [18]. Another way, which is the one considered in this work, is the possible reduction of GB resistivity by the addition of dopants.

It is now clear that GB properties highly depend on the GB structure [19–22]. A GB is determined by 5

macroscopic degrees of freedom. In the coincidence-site lattice (CSL) model, three of these parameters are grouped as a misorientation between the two crystals, given by an axis $\hat{a} = [uvw]$ and an angle θ. These translate into a particular Σ value, defined as the inverse of the coincidence-site density. The remaining two parameters correspond to the direction $\hat{n}$ of one of the crystals at the boundary plane and are given as a set of Miller indices (hkl). Therefore, several different GB structures are possible for a given Σ value. The GBs for which the boundary plane represents a plane of mirror symmetry are called twin boundaries. Of particular interest is the coherent twin boundary, a $\Sigma 3$ GB which is known for its significantly lower energy [23] and resistivity [24]. The CSL model has been widely adopted to characterize GBs with the introduction of scanning-electron-microscopy-based electron backscatter diffraction (SEM-EBSD)/orientation imaging microscopy (OIM), a computer-assisted and fully automated technique allowing the determination of the grain-boundary character distribution [25].

Typical samples of bulk recrystallized copper [26–28] or grain-boundary-engineered copper [29,30] display fractions of $\Sigma 3$ GBs of the order of 40% to 60%, a few percents of the related $\Sigma 9$ and $\Sigma 27$ GBs, while the remaining fraction of the GB population is distributed between low-angle GBs, other Σ GBs, and random GBs. Only a fraction of all the $\Sigma 3$ GBs are coherent twin boundaries, and they are found to represent 45% of the $\Sigma 3$ population in a set of nanocrystalline copper thin films [31]. Combining this information with an average 50% of $\Sigma 3$ GBs allows us to estimate that coherent twin boundaries can represent about 25% of all GBs in the material. However, the grain-boundary character distribution is strongly influenced by the processing method. The population of GBs in cold rolled copper can be fine tuned by low temperature anneal to reach 81% of observed $\Sigma 3$ GBs, of which 68% are found to be coherent twin boundaries, yielding a total fraction of 55% of coherent twin boundaries [32]. On the other hand, grain-boundary engineering does not help with increasing this total fraction as most of the $\Sigma 3$ GBs generated in copper after the treatment are not coherent twin boundaries [29].

In damascene copper interconnects—the present interconnect technology, additional parameters come into play as the material is now constrained in trenches on a substrate. Trench dimensions, bottom and sidewall substrate texture, electroplating, and annealing conditions all affect the microstructure to various degrees [33]. Importantly, for the downscaling, it is observed that the proportion of low-Σ CSL GBs drops substantially with decreasing linewidth [34]. The fraction of $\Sigma 3$ GBs decreases from more than 60% at a 2-μm linewidth, a typical fraction in bulk recrystallized copper, to about 10% around 0.14 μm [33,35]. The population of low-angle GBs remaining small in both cases, this decrease must be compensated by a corresponding increase in the frequency of higher Σ CSL GBs and random GBs. In a separate study, the fraction of coherent twin boundaries among $\Sigma 3$ GBs in damascene copper interconnects was estimated at 62% [36]. One should, therefore, expect the total fraction of coherent twin boundaries to be no larger than a few percent in submicrometer interconnects.

To qualitatively estimate the resistance of a material based on its microstructure, knowledge of the contribution from individual GBs is required [37]. The resistivity of the coherent twin boundary in copper is estimated at $0.17 \times 10^{-12}\ \Omega\,\mathrm{cm}^2$ [24]. Recently, the first measurements on single-GB resistivity were made using four-probe scanning tunneling microscopy (STM) and the high, measured resistivity of random GBs was contrasted with the much lower, calculated resistivity of high-angle GBs from the CSL model [38]. From a modeling perspective, *ab initio* calculations of GB resistivity were performed systematically on CSL GBs and tied to area-specific quantities such as the inverse atomic density in the boundary plane and the interfacial energy [39]. A rough classification of GBs in terms of resistivity emerges from those observations: the coherent twin boundary has the lowest known resistivity of all GBs; other twin GBs are found 1 order of magnitude higher and above; finally, random GBs display resistivities at least 2 orders of magnitude higher than the coherent twin boundary. The importance of twin boundaries for low material resistivity is supported by the recent study of nanotwinned Cu, where the resistivity of samples with small twin spacings of 15 nm was found to be 1.75 $\mu\Omega\,\mathrm{cm}$, only slightly larger than that of coarse-grained Cu [18]. Reducing twin-boundary density at a similar grain size with larger twin spacings resulted in a resistivity jump to 2.12 $\mu\Omega\,\mathrm{cm}$, as well as a net increase of the effective reflection coefficient r from the Mayadas-Schatzkes model [18]. Therefore, the changes to the microstructure of damascene copper interconnects as the dimensions scale down should have a substantial impact: the higher fraction of high-Σ and random GBs should increase the average GB resistivity, which in turn should result in a net increment in resistivity.

The design by grain-boundary engineering [40,41] of copper interconnects with a GB distribution favoring low-resistivity GBs, particularly coherent twin boundaries, is thus a first possible approach to addressing this problem. The next logical step to limit GB scattering in the size-effect regime would be to consider GB segregation and its possible use to mitigate GB resistivity. Indeed, grain-boundary segregation engineering [42], which will also be referred to as GB doping in this paper, has emerged in the recent past as a solution to improving the original properties of a material. It is our goal here to determine if GB segregation can have a positive effect on GB scattering, similar in a way to how surface coating can improve over surface scattering [43,44]. To do so, state-of-the-art

first-principles electronic-transport calculation methods will be employed.

In Sec. II, the recently introduced NEGF-DFT/NECPA method will be briefly presented as the method of choice for the treatment of disorder in electronic structure and transport calculations. Next, in Sec. III, the resistivity of doped copper bulk will then be computed for selected elements of the periodic table in order to assess the accuracy of the method, and to determine which elements can be used for GB doping without compromising too much on bulk resistivity. Finally, in Sec. IV, the concept of GB segregation and the possibility of GB doping will be debated. The resistivity of several copper GBs with various dopant concentrations will be calculated and the results discussed.

II. NEGF-DFT/NECPA METHOD

Throughout this work, use is made of nonequilibrium Green's functions (NEGF), implemented within the density functional theory (DFT), to compute the electronic and transport properties of the materials from a first-principles, parameter-free approach [45–47]. Disorder in the material is treated with the recently developed nonequilibrium coherent potential approximation (NECPA) [48]. The quantum transport package NANODSIM [49] is used for this purpose. The method was already successfully applied to the study of surface roughness [50] and surface coating [43] of copper thin films, GB scattering in copper single GBs [39], as well as to a variety of materials where disorder plays important roles [51–53].

A brief introduction to the method is given here. In NEGF-DFT, the Hamiltonian $\mathbf{H}$ of an ordered system is first calculated on a particular basis, in our case linear muffin-tin orbitals within the atomic-sphere approximation. The retarded and advanced Green's function $\mathbf{G}^{r,a}$ of the scattering region of a two-probe transport structure can then be determined as

$$\mathbf{G}^{r,a}(E) = [E\mathbf{O} - \mathbf{H} - \Sigma^{r,a}(E)]^{-1}, \tag{4}$$

where $\mathbf{O}$ is the overlap matrix and $\Sigma^{r,a}$ are the retarded and advanced self-energies, computed directly from the surface Green's function of the semi-infinite electrodes. The lesser self-energy $\Sigma^{<}$ can be decomposed in its left and right electrode contributions:

$$\begin{aligned}\Sigma^{<}(E) &= \Sigma_l^{<}(E) + \Sigma_r^{<}(E) \\ &= if_l(E)\mathbf{\Gamma}_l(E) + if_r(E)\mathbf{\Gamma}_r(E),\end{aligned} \tag{5}$$

where the Fermi-Dirac function of the left and right leads $f_{l,r}$ are expressed in terms of the electrochemical potentials $\mu_{l,r}$ and temperature T:

$$f_{l,r}(E) = [\exp(E - \mu_{l,r}/k_{\mathrm{B}}T) + 1]^{-1} \tag{6}$$

and the linewidth functions $\Gamma_{l,r}$ describing the coupling of the scattering region with the electrode are given by

$$\mathit{\Gamma}_{l,r}(E) = i[\Sigma_{l,r}^{r}(E) - \Sigma_{l,r}^{a}(E)]. \tag{7}$$

The lesser Green's function $\mathbf{G}^{<}$ is calculated via the Keldysh equation:

$$\mathbf{G}^{<}(E) = \mathbf{G}^{r}(E)\Sigma^{<}(E)\mathbf{G}^{a}(E). \tag{8}$$

Finally, the density matrix ρ is obtained as

$$\rho = -\frac{i}{2\pi}\int \mathbf{G}^{<}(E)dE. \tag{9}$$

In the low bias approximation where $f_l(E) \approx f_r(E) = f(E)$, Eq. (8) simplifies to

$$\mathbf{G}^{<}(E) = -f(E)[\mathbf{G}^{r}(E) - \mathbf{G}^{a}(E)]. \tag{10}$$

Once convergence is reached after the self-consistent NEGF-DFT iteration cycle, the transmission coefficients can be calculated as

$$T(E) = \mathrm{Tr}[\mathbf{\Gamma}_l(E)\mathbf{G}^{r}(E)\mathbf{\Gamma}_r(E)\mathbf{G}^{a}(E)] \tag{11}$$

and the conductance is then

$$G = \frac{2e^2}{h}\int dET(E)[f_l(E) - f_r(E)], \tag{12}$$

which is simplified at equilibrium as

$$G = \frac{e^2}{h}T(E_F). \tag{13}$$

As seen, the solution of $\mathbf{G}^{r,a}$ and $\mathbf{G}^{<}$ is essential to the determination of the electronic and transport properties of our system. To include the effect of disorder analytically, disorder averages are performed directly at the Green's function level, which is denoted with an overline. The determination of $\overline{\mathbf{G}^{r,a}}$ and $\overline{\mathbf{G}^{<}}$ are the main conditions for a transport formalism of disordered systems.

To do so, the Hamiltonian $\mathbf{H}$ of the scattering region is first decomposed into an off-diagonal definite part $\mathbf{H}_0$ and a diagonal random part ε of on-site energies. The retarded and advanced Green's function now read

$$\mathbf{G}^{r,a}(E) = [E\mathbf{O} - \mathbf{H}_0 - \varepsilon - \Sigma^{r,a}(E)]^{-1}. \tag{14}$$

The following disorder average must now be evaluated:

$$\overline{\mathbf{G}^{r,a}(E)} = \overline{[E\mathbf{O} - \mathbf{H}_0 - \varepsilon - \Sigma^{r,a}(E)]^{-1}}. \tag{15}$$

The calculation of the above formula can be done using the well-established coherent potential approximation

(CPA) [54,55]. In CPA, a coherent potential $\tilde{\varepsilon}^{r,a}$ is defined as

$$\overline{\mathbf{G}^{r,a}(E)} = [E\mathbf{O} - \mathbf{H}_0 - \tilde{\varepsilon}^{r,a}(E) - \Sigma^{r,a}(E)]^{-1}. \quad (16)$$

In the low bias approximation, $\overline{\mathbf{G}^{<}}$ simply reduces to

$$\overline{\mathbf{G}^{<}(E)} = -f(E)[\overline{\mathbf{G}^{r}(E)} - \overline{\mathbf{G}^{a}(E)}]. \quad (17)$$

Therefore, the iterative solution of $\tilde{\varepsilon}^{r,a}$ yields $\overline{\mathbf{G}^{r,a}}$, and by extension the electronic and transport properties of a disordered system in equilibrium.

However, the following more-complex disorder average must be solved to obtain $\overline{\mathbf{G}^{<}}$ when out of equilibrium, i.e., when $f_l(E) \neq f_r(E)$:

$$\overline{\mathbf{G}^{<}(E)} = \overline{\mathbf{G}^{r}(E)\Sigma^{<}(E)\mathbf{G}^{a}(E)}. \quad (18)$$

This was first achieved by defining and evaluating a nonequilibrium vertex correction (NVC) self-energy Λ due to the multiple impurity scattering [56]:

$$\overline{\mathbf{G}^{<}(E)} = \overline{\mathbf{G}^{r}(E)}\Sigma^{<}(E)\overline{\mathbf{G}^{a}(E)} + \overline{\mathbf{G}^{r}(E)}\Lambda(E)\overline{\mathbf{G}^{a}(E)}. \quad (19)$$

The nonequilibrium coherent potential approximation (NECPA) was more recently devised as an equivalent but more general approach to deal with disorder scattering at noneqiulibrium [48]. There, use is made of the generalized Langreth theorem to enable analytic continuation of the inverse of contour-ordered quantities [48]. Performing the disorder average of $\mathbf{G}$ as done in the CPA, it is found by analytic continuation of $\bar{\mathbf{G}}$ that

$$\overline{\mathbf{G}^{<}(E)} = \overline{\mathbf{G}^{r}(E)}\Sigma^{<}(E)\overline{\mathbf{G}^{a}(E)} + \overline{\mathbf{G}^{r}(E)}\tilde{\varepsilon}^{<}(E)\overline{\mathbf{G}^{a}(E)}, \quad (20)$$

where $\tilde{\varepsilon}^{<}(E)$ is the lesser coherent potential. It is shown that quantities Λ and $\tilde{\varepsilon}^{<}$ are in fact strictly equivalent [48].

III. RESISTIVITY OF DOPED BULK COPPER

The CPA and/or NECPA theories are essentially effective medium theories where atomic disorder is approximated by disorder averages at the Green's function level. As such, certain types of disorder are neglected, including impurity clustering, formation of ordered compounds and precipitation, etc. In practical implementations of the CPA/NECPA methods, so far the atomic-sphere approximation is used to allow the insertion of impurities on the atomic sites where an atomic sphere is defined. In close-packed structures such as the face-centered cubic lattice of copper, these atomic spheres are usually placed on the lattice sites themselves, without the need for the so-called empty spheres. This means that the impurity doping is substitutional. Before investigating the complex problem of GB doping, in this section we demonstrate the accuracy of our first-principles approach by investigating the simpler case of bulk doping.

The concept of using copper alloys with a minimal sacrifice on resistivity to gain reliability, such as improved adhesion, corrosion resistance, diffusion barrier properties, and electromigration, was discussed [57–59]. A list of criteria was established to systematically eliminate possible alloying elements for copper, starting with obvious reasons such as natural occurrence, radioactivity, toxicity, and then moving on to other considerations such as solubility, residual resistivity, etc. This selection process arrived at a set of 16 potential elements. Of those, ten were labeled as high-priority alloying elements for copper interconnect applications: Pd, Au, Al, Ag, Nb, Cr, B, Ti, In, and Mn. The remaining six elements marked with lower priority were Zn, V, C, Mg, P and Sn [60]. In the present work, a subset of the elements for which resistivity data are available [57,60] is chosen to test the accuracy of our first-principles NEGF-DFT/NECPA method, even if some of those are not part of the 16 suggested alloying elements for copper. Explicitly, those are Ag, Zn, Cd, Be, Mg, Pd, Al, In, Ni, B, Ga, Si, Sn, Ge, Co, and Ti, i.e., elements with s, p, and d orbital electrons.

For the calculation, a value of $a = 3.64$ Å is taken as the lattice constant of copper, as obtained previously [39]. The transmission is computed along the $\langle 100 \rangle$ direction. In the two-probe transport-structure setup, seen in Fig. 1, two pure-copper electrodes contact a central scattering region. The scattering region is decomposed into two pure-copper buffers, one directly in contact with the left electrode and the other with the right electrode, and a section of impurity-doped bulk copper sandwiched between these buffers.

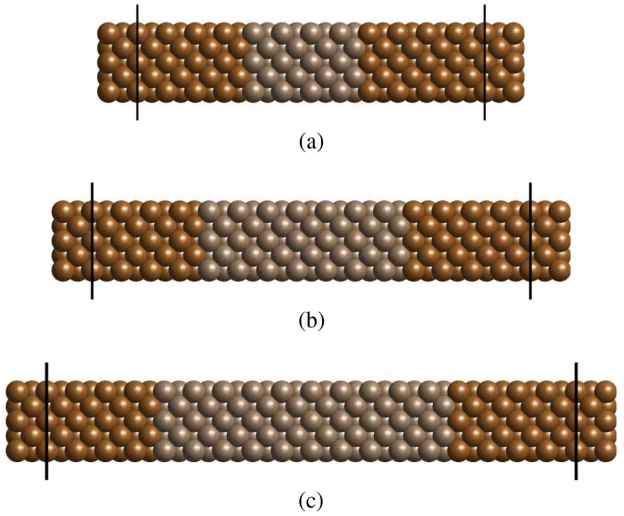

FIG. 1. Two-probe transport-structure setups with (a) 8, (b) 14, and (c) 20 doped copper monolayers. Two pure-copper bulk electrodes (dark brown) contact a scattering region defined by contact planes (dark lines). Pure-copper buffers (dark brown) extend the electrodes inside the scattering region, sandwiching an impurity-doped copper section (light brown).

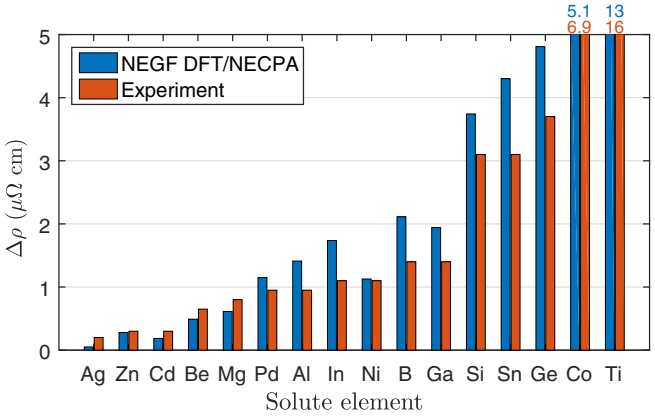

FIG. 2. The calculated residual resistivity $\Delta\rho$ for various solute elements at 1 at. % in bulk copper (blue) and measured experimental values in Refs. [57,60] (red). The consistency is qualitatively excellent and quantitatively reasonable.

In the doped bulk copper region, the impurity concentration is 1 at. %. Pure-copper buffers of eight monolayers are determined to be sufficient for the interatomic part of the electrostatic potential, known as Madelung potential, to converge to its bulk value at the contact with the pure-copper electrodes, away from the interface between pure and doped regions. Similarly, bulk conditions are recovered in the middle of the doped section when it spans eight monolayers or more. The section of doped copper bulk is then progressively extended to 10, 12, 14, 16, 18, and 20 monolayers, as sketched in Fig. 1. For each case the resistance R is calculated from the transmission coefficient, which allows us to determine the resistivity ρ by linear regression based on Ohm's law:

$$R = \rho \frac{l}{A}, \tag{21}$$

$$\rho = A \frac{dR}{dl}, \tag{22}$$

where l is the length of the scattering region and A its cross section. By taking its derivative, the constant contribution to R from the Sharvin resistance R_S [61] is eliminated. The bulk scattering region being free from other defects such as vacancies, dislocations, GBs, and from temperature effects, the residual resistivity (RR) $\Delta\rho$ due only to impurity scattering is thus directly obtained. It is important to emphasize that in the NVC/NECPA theories, the incoherent disorder averaging process—i.e., the contributions of the NVC self-energy [56] Λ or the lesser coherent potential [48] $\tilde{\varepsilon}^<$ discussed above, play a critical role leading up to the Ohm's law of resistance.

The calculated $\Delta\rho$ for the 16 alloying elements are displayed in Fig. 2 where they are compared with available experimental data. The deviation between the theoretical and experimental results fluctuates, with an average difference of about 30% over all the impurities. The qualitative trend is globally very well predicted by our calculations, confirming the promising alloying elements with $\Delta\rho \approx 1\ \mu\Omega\,\mathrm{cm}$ or below as Al, Zn, Cd, Be, Mg, Pd, Al, In, and Ni. Considering both the approximations in theory and error margins in the experiment, the consistency of the RR across this set of impurities is quite satisfactory.

IV. RESISTIVITY OF DOPED COPPER GB

Having verified our calculation methods with bulk copper alloying in the last section, we now investigate the effects of impurity doping on the electronic transport in copper GBs. We review the concepts of GB complexion and GB segregation in a first part, then present and analyze the transport results in a second part.

While interfaces such as GBs can be characterized by equilibrium thermodynamics, equilibrium interface states are inhomogeneous with possible gradients in structure, composition, and other properties. Such interfaces also cannot exist independently of their abutting bulk phases. For those reasons, they must be distinguished from conventional phases and the term complexion was adopted to represent interfacial material in thermodynamical equilibrium with its abutting phase(s) [62–64]. Complexions can have multiple characters, being made of a pure single element (intrinsic) or containing a certain amount of adsorbed solute (extrinsic), and having various degrees of structural and chemical order. Similar to bulk phase transitions, they may undergo transformations. A congruent transition conserves the GB character, while faceting or dissociation decomposes a complexion into two. Complexion transitions are predicted in intrinsic metallic GBs both by experimental measurements [65] and atomistic computer simulations [66], as a result of the variation of temperature or the introduction of defects. This gives rise to different metastable phases such as various kite-shaped structures in copper [66,67].

The presence of impurities in extrinsic complexions adds a whole new level of complexity to the problem, but at the same time this new degree of freedom offers possibilities to improve over the properties of intrinsic complexions. In the case of GBs, the addition of impurities can be done by GB segregation. A polycrystalline material will tend to reduce its total energy by the interaction of GBs with other defects like solute or impurity atoms [68], such that these atoms will accumulate at GBs: this is GB segregation [69]. More precisely, the width of a GB being of the nanometer scale, GB segregation can be called nanosegregation to distinguish with other segregation processes happening on larger scales. Based on the conversion of the GB width to a finite number of atomic layers, six Dillon-Harmer discrete GB complexions are categorized: the submonolayer (almost "clean" GB), the monolayer, the bilayer, the trilayer, the amorphous intergranular film, and the wetting intergranular film. An example of submonolayer and monolayer GB complexion is found in Fig. 3. Several of those Dillon-Harmer GB

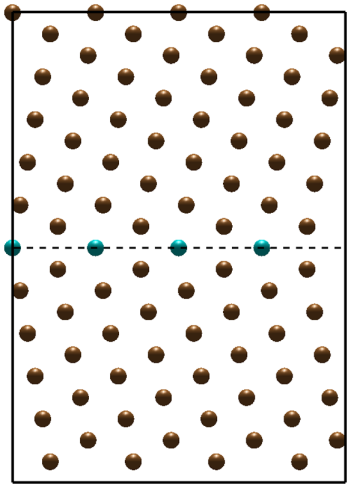

FIG. 3. GB complexion in the Σ11 GB. For the submonolayer model, the atomic sites of the boundary plane (light blue) contain dopants at concentration c and copper atoms at concentration $1-c$, while atomic sites of the grains (dark brown) contain only copper. For the monolayer model, the atomic sites of the boundary plane contain strictly dopants.

complexions have been observed using aberration-corrected high-angle annular dark-field scanning transmission electron microscopy (STEM) [62,70–72] and are also well predicted by atomistic computer simulations [67].

GB segregation has an important impact on the material properties. It can be used to control the grain growth and grain size of nanocrystalline alloys [73–76]; zirconium is, for example, an excellent candidate to stabilize nanocrystalline copper [77]. Mechanical effects have been well studied, like impurity-induced embrittlement by bismuth in copper [70,78] or GB sliding resistance [79]. The modeling of defect generation and diffusion at GBs showed that certain dopants such as B, C, and P can be beneficial to copper interconnects by slowing electromigration [59,80,81]. However, little is known of the impact that GB segregation can have on electronic-transport properties. After verifying its accuracy in the previous section with the simpler case of copper bulk doping, we now apply the NEGF-DFT/NECPA first-principles method to evaluate the effect of impurities on the resistance in copper GBs.

For the calculation of the specific resistivity γ_R of doped copper GBs, the attention will be focused on six twin GBs: the Σ3, Σ5, Σ9, Σ11, Σ13a, and Σ17a. These particular GBs are chosen for their relative simplicity as well as small periodic unit cell, which allows us to keep computational costs at their minimum. The atomic structure of each GB was relaxed into its equilibrium state via total energy minimization, and the structural, energetic, and transport properties were studied in a previous work [39]. Importantly, the γ_R of those GBs is known. In terms of Dillon-Harmer GB complexion, only the submonolayer and monolayer GB complexions were considered. An example is given for the Σ11 GB in Fig. 3. Multilayer GB segregation could occur, but this might be accompanied by profound structural changes in the GB core at high impurity concentrations and is not considered in this work. To simulate the submonolayer GB complexion, the concentration c of impurities on each atomic site of the boundary plane can be continuously modified from 0 (i.e., 0 at. % of impurity) to 1 (i.e., 100 at. % of impurity) thanks to the NEGF-DFT/NECPA method. The concentration spectrum is explored here by varying c from 0.1 to 0.9 in increments of 0.2. The monolayer GB complexion is investigated using the self-consistent NEGF-DFT formalism as discussed above.

The γ_R results as a function of dopant and concentration are shown in Fig. 4 for the various GBs in the case of a submonolayer GB complexion. As the plot in Fig. 4(a) indicates, the addition of impurities to the coherent twin boundary Σ3 is always detrimental to γ_R. The average spread between different c given a fixed dopant is the largest for this GB, revealing that the coherent twin boundary is particularly sensitive to doping. The γ_R of the pure coherent twin boundary being extremely small, only 0.17×10^{-12} Ω cm^2, the increase caused by doping is highly detrimental there, resulting in a γ_R larger by more than 1 order of magnitude in the worst-case scenario. For the Σ5, Σ9, and Σ11 GBs, a similar picture is seen where most of the tested dopants lead to a γ_R increase across the concentration spectrum. Globally, in those first four GBs, the trend observed in γ_R as a function of the dopant is very similar to that of ρ in the case of copper bulk doping. However, it is interesting to note that for the particular case of the Σ9 GB, a γ_R slightly smaller than its pure-copper counterpart is observed for Zn, Cd, Be, Al, B, and Ga at certain concentrations, glimpsing the possibility of reduced resistivity. This becomes apparent in the case of the last two GBs, Σ13a and Σ17a shown in Figs. 4(e) and 4(f), where γ_R is found to be smaller than the nominal value for multiple elements and concentrations. In Σ17a, eight elements display this feature: Zn, Cd, Be, Mg, Al, In, B, and Ga. In Σ13a, three additional elements show the potential for reduced resistivity: Si, Sn, and Ge. Those 11 elements can be further split into two categories. Some of them are found to systematically decrease γ_R over the concentration range, those are explicitly Zn, Cd, Be, and Mg. The other elements show a decrease limited to certain GBs and concentrations, mostly toward the low-to-medium range of c.

The reduced resistivity by doping for higher Σ GBs is remarkable. The reduction factor almost reaches 50% for the Σ13a GB at particular dopant concentrations. If the trend is followed at even higher Σ GBs (possibly random GBs), and depending on the material microstructure, GB doping could therefore lead to a net and significant decrease of GB scattering. After considering the observations made about the microstructure of copper interconnects in the previous section, they appear to be very likely candidates for such a reduction. In fact, decreasing GB

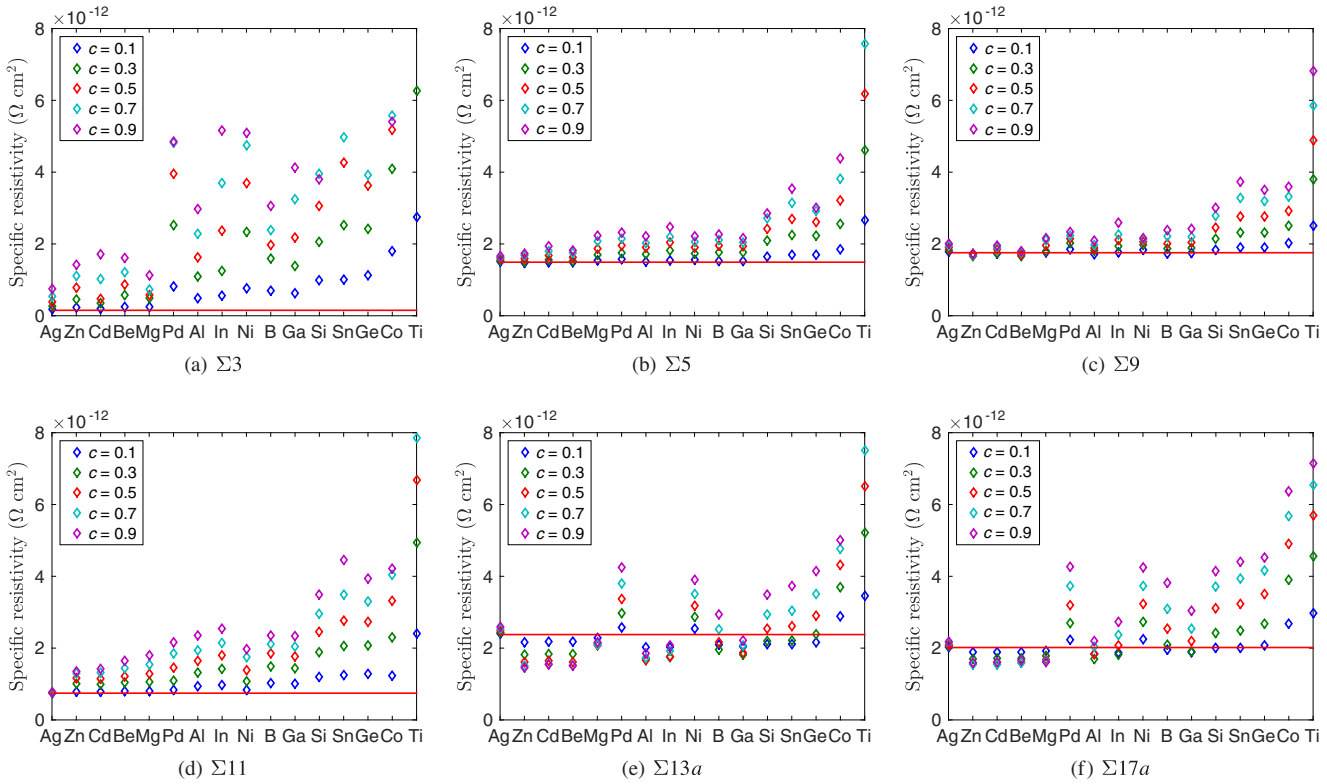

FIG. 4. Specific resistivity γ_R of the (a) Σ3, (b) Σ5, (c) Σ9, (d) Σ11, (e) Σ13a, and (f) Σ17a GBs for a submonolayer GB complexion with concentration c ranging from 10% to 90%. The red line corresponds to the γ_R of equivalent pure-copper GB.

resistivity with increasing impurity content was observed in the case of Al [82], which is one of the elements for which reduced resistivity is predicted here.

Additionally, a connection with GB segregation enthalpy can be established. The value of this enthalpy is tabulated for a very large number of binary systems following a Miedema-type model parametrized to represent the average GB behavior in each particular material [83]. In this model, positive values of the enthalpy represent the tendency of the dopant to segregate to the GB, while a negative value indicates antisegregation, that is the depletion of the dopant in the GB. The model might be inaccurate in the low-Σ limit of the GB spectrum, however, it should be applicable to GBs with an average character. And indeed, while a bulklike increase in resistivity is seen in the doped Σ3, Σ5, Σ9, and Σ11 GBs irrespectively of segregation enthalpy, a strong correlation between resistivity and segregation enthalpy is otherwise observed in the doped Σ13a and Σ17a GBs. Elements with a known positive enthalpy Ag, Zn, Mg, Al, and Si almost systematically yield a reduced resistivity in the Σ13a and Σ17a, with the exception of Ag. On the other hand, all of the elements with known negative enthalpy, namely Pd, Ni, Co, and Ti, result in a detrimental increase to resistivity. This outlines once again a connection between energy and transport properties of GBs, and suggests the possibility of a self-limiting process where GB segregation occurs preferentially to boundary types which, in fact, exhibit a resistivity reduction.

To further assess the possibility of reduced GB resistivity, the calculation of γ_R as a function of the selected dopants is performed and shown in Fig. 5 for the various GBs in the case of a monolayer GB complexion. This essentially allows us to rely on the traditional NEGF-DFT method (since there is no disorder) and to provide further verification of the results. Once again, a trend similar to that of copper bulk doping is found for the first four GBs, namely Σ3, Σ5, Σ9, and Σ11. For those GBs, the resistivity is at best close to that of pure-copper GBs with Zn and Be. On the other hand, a clear decrease in γ_R is observed for the Σ13a and Σ17a for several elements as was the case with the submonolayer complexion. Particularly, Zn, Cd, Be, and Mg again yield a reduced resistivity in both GBs. While the monolayer is close to optimal in terms of resistivity reduction for Zn, Cd, Be, and Mg, it is outperformed by the submonolayer for the other elements where a decrease is sometimes only possible at lower dopant concentrations.

To gain a better understanding of these results, the projected density of states (PDOS) is calculated across the scattering region at the Fermi energy E_F and is compared with the average charge distribution, where the average charge is defined as the disorder-averaged difference between the self-consistently calculated valence charge and the standard valence charge of the

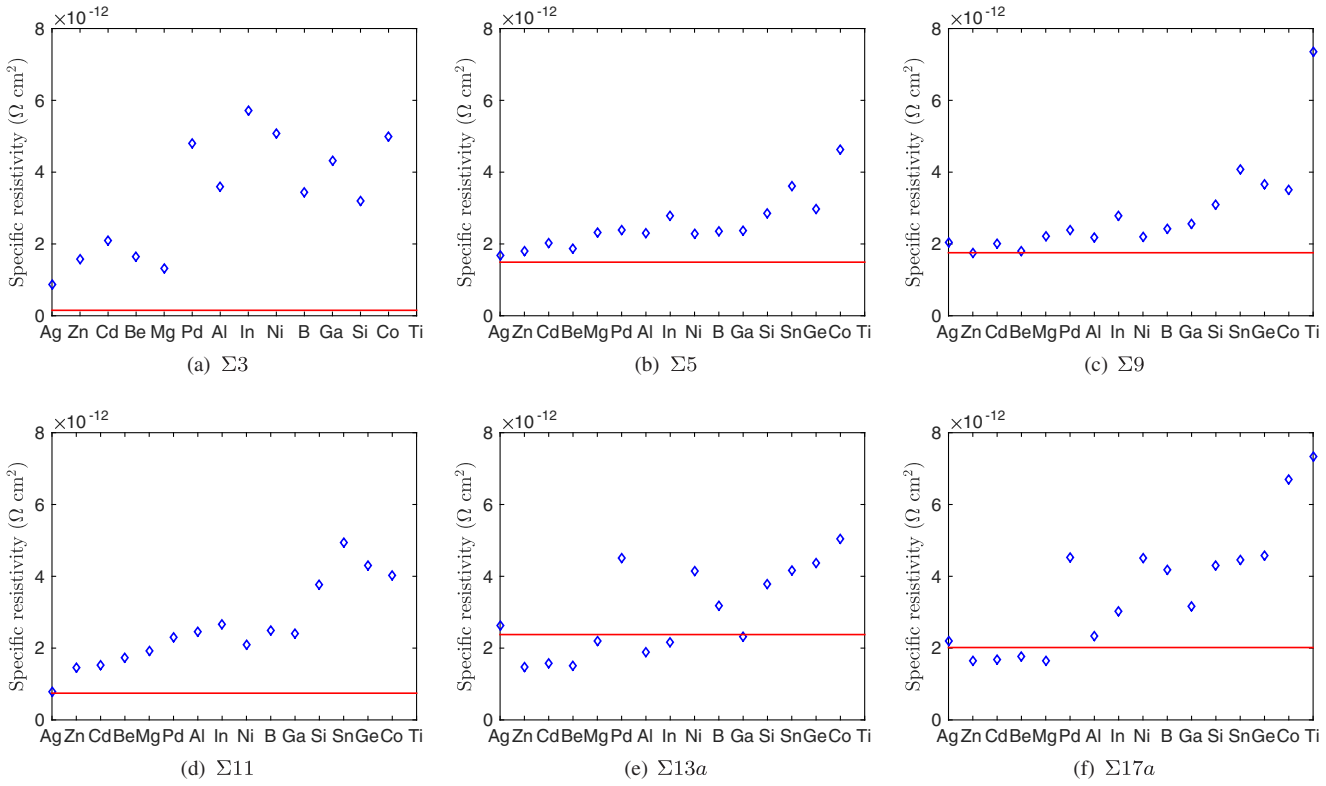

FIG. 5. Specific resistivity γ_R of the (a) Σ3, (b) Σ5, (c) Σ9, (d) Σ11, (e) Σ13a, and (f) Σ17a GBs for a monolayer GB complexion. The red line corresponds to the γ_R of equivalent pure-copper GB.

corresponding atomic element. This is done first in the case of two pure GBs, Σ3 and Σ13a. As seen in Fig. 6, total PDOS and average charge distribution are well matched, meaning that very few states are left available for scattering. This has for a consequence the extremely small resistivity that is characteristic of the coherent twin boundary. On the opposite, the creation of a number of interfacial states at the boundary plane is observed in the total PDOS of the Σ13a while the region becomes simultaneously charge depleted. This means that a lot of the interfacial states are left empty

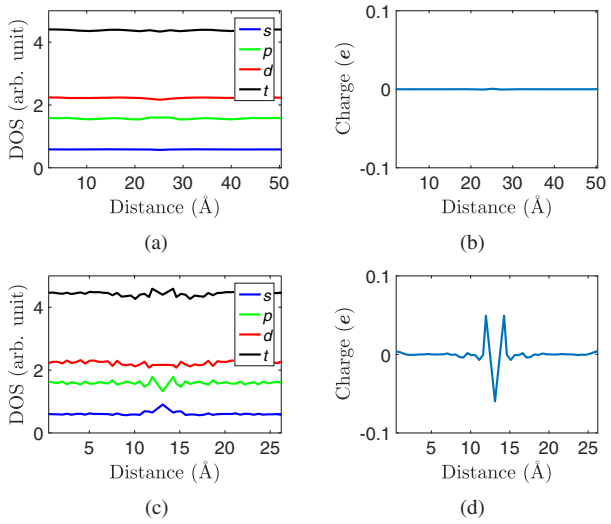

FIG. 6. (a) PDOS and (b) average charge distribution for the Σ3 GB; (c) PDOS and (d) average charge distribution for the Σ13a GB. The total (black) PDOS is decomposed into s (blue), p (green), and d (red) orbital contributions.

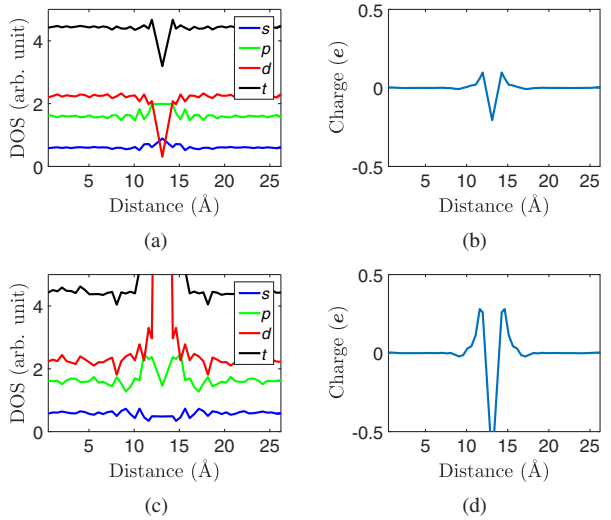

FIG. 7. (a) PDOS and (b) charge distribution for the Σ13a GB with Zn monolayer complexion; (c) PDOS and (d) charge distribution for the Σ13a GB with Ti monolayer complexion. The total (black) PDOS is decomposed into s (blue), p (green), and d (red) orbital contributions.

and can thus contribute to scattering, increasing the GB resistivity in this way.

The PDOS at E_F and charge distribution are then computed for the Zn-doped and Ti-doped $\Sigma 13a$ GB with a monolayer GB complexion. The results are displayed in Fig. 7. In the case of Zn doping, a gap is now introduced in the total PDOS at the boundary plane that matches with the charge distribution in that region. By reducing the number of states available at that particular energy, the effective number of empty states is reduced, which supports the low specific resistivity previously observed with Zn. In the case of Ti doping, on the other hand, a huge number of impurity states is created around the boundary plane by the insertion of Ti atoms while the region suffers charge depletion at the same time. This translates in the large increase of specific resistivity observed in the GB with the addition of Ti.

V. SUMMARY

Using the state-of-the-art self-consistent NEGF-DFT/NECPA first-principles method, we have calculated and investigated resistivity of impurity-doped copper. The calculated resistivity of doped bulk copper for 16 doping elements at concentration 1 at. % is in qualitatively excellent and quantitatively reasonable agreement with the corresponding experimental data, and allow us to determine Ag, Zn, Mg, Pd, Al, and In as best candidates for GB doping. These atoms have a minimal impact on the bulk resistivity while also conforming to a set of established criteria for alloying with copper. The specific resistivity of six twin GBs is determined for those elements over a wide spectrum of doping concentrations for two Dillon-Harmer GB complexions, namely the submonolayer and the monolayer GB complexions. Reduced resistivity is observed for Zn, Mg, Al, In, and other elements in two high-Σ GBs, and is qualitatively related to the segregation enthalpy as well as to a low number of empty states around the Fermi energy in the boundary plane region of the GB. This leads to the possibility of net reduced resistivity depending on the material microstructure. The noticeably large proportion of high-Σ and random GBs in copper interconnects with small, submicrometer dimensions make them particularly good candidates to such a resistivity reduction via GB doping.

ACKNOWLEDGMENTS

The authors thank Professor K. Dunn for useful discussions. This work is supported by the Semiconductor Research Corporation through the FAME STARnet Center and the Center for Advanced Interconnect Systems Technologies under Contract No. 1292.078. M. C. and H. G. gratefully acknowledge financial support from FQRNT of Québec and NSERC of Canada. We are grateful to Calcul-Québec and Compute Canada for providing substantial computational resources which made this work possible.

[1] T. S. Kuan, C. K. Inoki, G. S. Oehrlein, K. Rose, Y. P. Zhao, G. C. Wang, S. M. Rossnagel, and C. Cabral, Fabrication and performance limits of sub-0.1 μm Cu interconnects, MRS Proc. **612**, D7.1.1 (2000).

[2] S. M. Rossnagel and T. S. Kuan, Alteration of Cu conductivity in the size effect regime, J. Vac. Sci. Technol. B **22**, 240 (2004).

[3] D. Josell, S. H. Brongersma, and Z. Tőkei, Size-dependent resistivity in nanoscale interconnects, Annu. Rev. Mater. Res. **39**, 231 (2009).

[4] G. Steinlesberger, M. Engelhardt, G. Schindler, W. Steinhgl, A. von Glasow, K. Mosig, and E. Bertagnolli, Electrical assessment of copper damascene interconnects down to sub-50 nm feature sizes, Microelectron. Eng. **64**, 409 (2002).

[5] G. Schindler, G. Steinlesberger, M. Engelhardt, and W. Steinhgl, Electrical characterization of copper interconnects with end-of-roadmap feature sizes, Solid State Electron. **47**, 1233 (2003).

[6] Y. Kitaoka, T. Tono, S. Yoshimoto, T. Hirahara, S. Hasegawa, and T. Ohba, Direct detection of grain boundary scattering in damascene Cu wires by nanoscale four-point probe resistance measurements, Appl. Phys. Lett. **95**, 052110 (2009).

[7] See the latest edition of the ITRS (International Technology Roadmap for Semiconductors), http://www.itrs2.net/.

[8] S. Kincal, M. C. Abraha, and K. Schuegraf, RC Performance evaluation of interconnect architecture options beyond the 10-nm logic node, IEEE Trans. Electron Devices **61**, 1914 (2014).

[9] A. F. Mayadas and M. Shatzkes, Electrical-resistivity model for polycrystalline films: The case of arbitrary reflection at external surfaces, Phys. Rev. B **1**, 1382 (1970).

[10] C. Durkan and M. E. Welland, Size effects in the electrical resistivity of polycrystalline nanowires, Phys. Rev. B **61**, 14215 (2000).

[11] T. Sun, B. Yao, A. P. Warren, K. Barmak, M. F. Toney, R. E. Peale, and K. R. Coffey, Surface and grain-boundary scattering in nanometric Cu films, Phys. Rev. B **81**, 155454 (2010).

[12] J. S. Chawla, F. Gstrein, K. P. O'Brien, J. S. Clarke, and D. Gall, Electron scattering at surfaces and grain boundaries in Cu thin films and wires, Phys. Rev. B **84**, 235423 (2011).

[13] W. Steinhögl, G. Schindler, G. Steinlesberger, and M. Engelhardt, Size-dependent resistivity of metallic wires in the mesoscopic range, Phys. Rev. B **66**, 075414 (2002).

[14] D. Josell, A paradigm for interconnect geometry to reduce grain boundary resistance, J. Appl. Phys. **100**, 123705 (2006).

[15] M. Traving, G. Schindler, and M. Engelhardt, Damascene and subtractive processing of narrow tungsten lines: Resistivity and size effect, J. Appl. Phys. **100**, 094325 (2006).

[16] V. Carreau, S. Maitrejean, Y. Brechet, M. Verdier, D. Bouchu, and G. Passemard, Cu grain growth in interconnects trenches—Experimental characterization of the overburden effect, Microelectron. Eng. **85**, 2133 (2008).

[17] K. Khoo, J. Onuki, T. Nagano, S. Tashiro, Y. Chonan, H. Akahoshi, T. Haba, T. Tobita, M. Chiba, and K. Ishikawa, Microstructures of 50-nm Cu interconnects along the longitudinal direction, Mater. Trans., JIM **48**, 2703 (2007).

[18] X. H. Chen, L. Lu, and K. Lu, Electrical resistivity of ultrafine-grained copper with nanoscale growth twins, J. Appl. Phys. **102**, 083708 (2007).

[19] K. T. Aust and B. Chalmers, Energies and structure of grain boundaries, *Metal Interfaces* (American Society for Metals, Cleveland, 1952), p. 153.

[20] P. V. Andrews, M. B. West, and C. R. Robeson, The effect of grain boundaries on the electrical resistivity of polycrystalline copper and aluminium, Philos. Mag. **19**, 887 (1969).

[21] A. P. Sutton and R. W. Balluffi, Overview no. 61 On geometric criteria for low interfacial energy, Acta Metall. **35**, 2177 (1987).

[22] I. Nakamichi, Electrical resistivity and grain boundaries in metals, Mater. Sci. Forum **207–209**, 47 (1996).

[23] D. L. Olmsted, S. M. Foiles, and E. A. Holm, Survey of computed grain boundary properties in face-centered cubic metals: I. Grain boundary energy, Acta Mater. **57**, 3694 (2009).

[24] L. Lu, Y. Shen, X. Chen, L. Qian, and K. Lu, Ultrahigh strength and high electrical conductivity in copper, Science **304**, 422 (2004).

[25] B. L. Adams, S. I. Wright, and K. Kunze, Orientation imaging: The emergence of a new microscopy, Metall. Trans. A **24**, 819 (1993).

[26] W. E. King and A. J. Schwartz, Toward optimization of the grain boundary character distribution in OFE copper, Scr. Mater. **38**, 449 (1998).

[27] A. J. Schwartz, M. Kumar, and W. E. King, Influence of processing method on the grain boundary character distribution and network connectivity, MRS Proc. **586**, 3 (1999).

[28] Y. Kaneno and T. Takasugi, Grain-boundary character distribution in recrystallized $L1_2$ ordered intermetallic alloys, Metall. Mater. Trans. A **34**, 2429 (2003).

[29] V. Randle, G. S. Rohrer, H. M. Miller, M. Coleman, and G. T. Owen, Five-parameter grain boundary distribution of commercially grain boundary engineered nickel and copper, Acta Mater. **56**, 2363 (2008).

[30] K. J. Al-Fadhalah, Texture and grain boundary character distribution in a thermomechanically processed OFHC copper, J. Eng. Mater. Technol. **134**, 011001 (2011).

[31] A. D. Darbal, K. J. Ganesh, X. Liu, S.-B. Lee, J. Ledonne, T. Sun, B. Yao, A. P. Warren, G. S. Rohrer, A. D. Rollett, P. J. Ferreira, K. R. Coffey, and K. Barmak, Grain boundary character distribution of nanocrystalline Cu thin films using stereological analysis of transmission electron microscope orientation maps, Microsc. Microanal. **19**, 111 (2013).

[32] V. Randle, P. Davies, and B. Hulm, Grain-boundary plane reorientation in copper, Philos. Mag. A **79**, 305 (1999).

[33] J.-Y. Cho, Texture and microstructure in Cu damascene interconnects, Ph.D. thesis, McGill University, Canada, 2004.

[34] K. Khoo and J. Onuki, Texture investigation in the trench depth direction of very fine copper wires less than 100 nm wide using electron backscatter diffraction, Thin Solid Films **518**, 3413 (2010).

[35] J.-Y. Cho, H.-J. Lee, H. Kim, and J. A. Szpunar, Textural and microstructural transformation of Cu damascene interconnects after annealing, J. Electron. Mater. **34**, 506 (2005).

[36] S. I. Wright and R. J. Larsen, Extracting twins from orientation imaging microscopy scan data, J. Microsc. **205**, 245 (2002).

[37] J. M. Rickman and K. Barmak, Simulation of electrical conduction in thin polycrystalline metallic films: Impact of microstructure, J. Appl. Phys. **114**, 133703 (2013).

[38] T.-H. Kim, X.-G. Zhang, D. M. Nicholson, B. M. Evans, N. S. Kulkarni, B. Radhakrishnan, E. A. Kenik, and A.-P. Li, Large discrete resistance jump at grain boundary in copper nanowire, Nano Lett. **10**, 3096 (2010).

[39] M. César, D. Liu, D. Gall, and H. Guo, Calculated Resistances of Single Grain Boundaries in Copper, Phys. Rev. Applied **2**, 044007 (2014).

[40] K. T. Aust, Grain boundary engineering, Can. Metall. Q. **33**, 265 (1994).

[41] T. Watanabe, Grain boundary engineering: Historical perspective and future prospects., J. Mater. Sci. **46**, 4095 (2011).

[42] D. Raabe, M. Herbig, S. Sandlbes, Y. Li, D. Tytko, M. Kuzmina, D. Pionge, and P.-P. Choi, Grain boundary segregation engineering in metallic alloys: A pathway to the design of interfaces, Curr. Opin. Solid State Mater. Sci. **18**, 253 (2014).

[43] F. Zahid, Y. Ke, D. Gall, and H. Guo, Resistivity of thin Cu films coated with Ta, Ti, Ru, Al, and Pd barrier layers from first principles, Phys. Rev. B **81**, 045406 (2010).

[44] P. Y. Zheng, R. P. Deng, and D. Gall, Ni doping on Cu surfaces: Reduced copper resistivity, Appl. Phys. Lett. **105**, 131603 (2014).

[45] J. Taylor, H. Guo, and J. Wang, *Ab initio* modeling of quantum transport properties of molecular electronic devices, Phys. Rev. B **63**, 245407 (2001).

[46] B. Larade, J. Taylor, H. Mehrez, and H. Guo, Conductance, I–V curves, and negative differential resistance of carbon atomic wires, Phys. Rev. B **64**, 075420 (2001).

[47] J. Taylor, H. Guo, and J. Wang, *Ab initio* modeling of open systems: Charge transfer, electron conduction, and molecular switching of a C_{60} device, Phys. Rev. B **63**, 121104 (2001).

[48] Y. Zhu, L. Liu, and H. Guo, Quantum transport theory with nonequilibrium coherent potentials, Phys. Rev. B **88**, 205415 (2013).

[49] J. Maassen, M. Harb, V. Michaud-Rioux, Y. Zhu, and H. Guo, Quantum transport modeling from atomic first principles, Proc. IEEE **101**, 518 (2013).

[50] Y. Ke, F. Zahid, V. Timoshevskii, K. Xia, D. Gall, and H. Guo, Resistivity of thin Cu films with surface roughness, Phys. Rev. B **79**, 155406 (2009).

[51] Y. Wang, F. Zahid, Y. Zhu, L. Liu, J. Wang, and H. Guo, Band offset of $GaAs/Al_xGa_{1-x}As$ heterojunctions from atomistic first principles, Appl. Phys. Lett. **102**, 132109 (2013).

[52] Y. Wang, H. Yin, R. Cao, F. Zahid, Y. Zhu, L. Liu, J. Wang, and H. Guo, Electronic structure of III-V zinc-blende semiconductors from first principles, Phys. Rev. B **87**, 235203 (2013).

[53] L. Zhang, F. Zahid, Y. Zhu, L. Liu, J. Wang, H. Guo, P. C. H. Chan, and M. Chan, First principles simulations of nanoscale silicon devices with uniaxial strain, IEEE Trans. Electron Devices **60**, 3527 (2013).

[54] P. Soven, Coherent-potential model of substitutional disordered alloys, Phys. Rev. **156**, 809 (1967).
[55] D. W. Taylor, Vibrational properties of imperfect crystals with large defect concentrations, Phys. Rev. **156**, 1017 (1967).
[56] Y. Ke, K. Xia, and H. Guo, Disorder Scattering in Magnetic Tunnel Junctions: Theory of Nonequilibrium Vertex Correction, Phys. Rev. Lett. **100**, 166805 (2008).
[57] S. P. Murarka and S. W. Hymes, Copper metallization for ULSI and beyond, Crit. Rev. Solid State Mater. Sci. **20**, 87 (1995).
[58] S. P. Murarka, Multilevel interconnections for ULSI and GSI era, Mater. Sci. Eng. R **19**, 87 (1997).
[59] K. H. Bevan, W. Zhu, H. Guo, and Z. Zhang, Terminating Surface Electromigration at the Source, Phys. Rev. Lett. **106**, 156404 (2011).
[60] K. Barmak, C. Cabral, K. P. Rodbell, and J. M. E. Harper, On the use of alloying elements for Cu interconnect applications, J. Vac. Sci. Technol. B **24**, 2485 (2006).
[61] G. E. W. Bauer, K. M. Schep, K. Xia, and P. J. Kelly, Scattering theory of interface resistance in magnetic multilayers, J. Phys. D **35**, 2410 (2002).
[62] S. J. Dillon, M. Tang, W. C. Carter, and M. P. Harmer, Complexion: A new concept for kinetic engineering in materials science, Acta Mater. **55**, 6208 (2007).
[63] M. P. Harmer, Interfacial kinetic engineering: How far have we come since Kingery's inaugural Sosman address?, J. Am. Ceram. Soc. **93**, 301 (2010).
[64] P. R. Cantwell, M. Tang, S. J. Dillon, J. Luo, G. S. Rohrer, and M. P. Harmer, Grain boundary complexions, Acta Mater. **62**, 1 (2014).
[65] S. V. Divinski, H. Edelhoff, and S. Prokofjev, Diffusion and segregation of silver in copper $\Sigma5(310)$ grain boundary, Phys. Rev. B **85**, 144104 (2012).
[66] T. Frolov, D. L. Olmsted, M. Asta, and Y. Mishin, Structural phase transformations in metallic grain boundaries, Nat. Commun. **4**, 1899 (2013).
[67] T. Frolov, S. V. Divinski, M. Asta, and Y. Mishin, Effect of Interface Phase Transformations on Diffusion and Segregation in High-Angle Grain Boundaries, Phys. Rev. Lett. **110**, 255502 (2013).
[68] P. C. Millett, R. P. Selvam, S. Bansal, and A. Saxena, Atomistic simulation of grain boundary energetics—Effects of dopants, Acta Mater. **53**, 3671 (2005).
[69] P. Lejcek, *Grain Boundary Segregation in Metals*, Springer Series in Materials Science Vol. 136 (Springer, Heidelberg, 2010).
[70] G. Duscher, M. F. Chisholm, U. Alber, and M. Rühle, Bismuth-induced embrittlement of copper grain boundaries, Nat. Mater. **3**, 621 (2004).
[71] J. Luo, H. Cheng, K. M. Asl, C. J. Kiely, and M. P. Harmer, The role of a bilayer interfacial phase on liquid metal embrittlement, Science **333**, 1730 (2011).
[72] A. Kundu, K. M. Asl, J. Luo, and M. P. Harmer, Identification of a bilayer grain boundary complexion in Bi-doped Cu, Scr. Mater. **68**, 146 (2013).
[73] R. Kirchheim, Grain coarsening inhibited by solute segregation, Acta Mater. **50**, 413 (2002).
[74] P. C. Millett, R. P. Selvam, and A. Saxena, Molecular dynamics simulations of grain size stabilization in nanocrystalline materials by addition of dopants, Acta Mater. **54**, 297 (2006).
[75] P. C. Millett, R. P. Selvam, and A. Saxena, Stabilizing nanocrystalline materials with dopants, Acta Mater. **55**, 2329 (2007).
[76] A. Detor and C. Schuh, Tailoring and patterning the grain size of nanocrystalline alloys, Acta Mater. **55**, 371 (2007).
[77] M. A. Atwater, R. O. Scattergood, and C. C. Koch, The stabilization of nanocrystalline copper by zirconium, Mater. Sci. Eng. A **559**, 250 (2013).
[78] R. Schweinfest, A. T. Paxton, and M. W. Finnis, Bismuth embrittlement of copper is an atomic size effect, Nature (London) **432**, 1008 (2004).
[79] P. C. Millett, R. P. Selvam, and A. Saxena, Improving grain boundary sliding resistance with segregated dopants, Mater. Sci. Eng. A **431**, 92 (2006).
[80] C.-L. Liu, Modeling and simulation for microelectronic materials research, Phys. Status Solidi B **226**, 47 (2001).
[81] C.-L. Liu, Screening beneficial dopants to Cu interconnects by modeling, Appl. Phys. Lett. **80**, 763 (2002).
[82] S. Yokogawa, H. Tsuchiya, Y. Kakuhara, and K. Kikuta, Analysis of Al doping effects on resistivity and electromigration of copper interconnects, IEEE Trans. Device Mater. Reliab. **8**, 216 (2008).
[83] H. A. Murdoch and C. A. Schuh, Estimation of grain boundary segregation enthalpy and its role in stable nanocrystalline alloy design, J. Mater. Res. **28**, 2154 (2013).